Soft Matter

Phantom chain simulations for fracture of star polymer networks with various strand densities

Journal:	*Soft Matter*
Manuscript ID	SM-ART-06-2024-000726.R2
Article Type:	Paper
Date Submitted by the Author:	12-Aug-2024
Complete List of Authors:	Masubuchi, Yuichi; Nagoya University, Materials Physics Ishida, Takato; Nagoya University, Materials Physics Koide, Yusuke; Nagoya University, Materials Physics Uneyama, Takashi; Nagoya University, Department of Materials Physics

Phantom chain simulations for fracture of star polymer networks with various strand densities

*Yuichi Masubuchi, Takato Ishida, Yusuke Koide, and Takashi Uneyama
Department of Materials Physics, Nagoya University, Nagoya 4649603, Japan

*To whom correspondence should be addressed mas@mp.pse.nagoya-u.ac.jp
Ver Aug 12, 2024

Abstract

Despite many attempts, the relation between fracture and structure of polymer networks is yet to be clarified. For this problem, a recent study for phantom chain simulations [Macromolecules, 56, 9359 (2023)] has demonstrated that the fracture characteristics obtained for polymer networks with various node functionalities and conversion ratios lie on master curves if they are plotted against cycle rank, which is the number of closed loops in the network per network node. In this study, we extended the simulation to the effect of prepolymer concentration c on the relationships between cycle rank and fracture characteristics within the concentration range of $1 \lesssim c/c^* \lesssim 10$, concerning the overlapping concentration c^*. We created networks from sols of star-branched phantom bead-spring chains via end-linking reaction between different chains through Brownian dynamics simulations with varying the number of branching arms f from 1 to 8, and the conversion ratio φ_c from 0.6 to 0.95. For the resultant networks, cycle rank ξ was consistent with the mean-field theory. The networks were uniaxially stretched with energy minimization until the break to obtain modulus G, strain at break ε_b, stress at break σ_b, and work for fracture W_b. With the branch point density υ_{br}, G/υ_{br}, ε_b, σ_b/υ_{br}, and W_b/υ_{br} of the data for various f and φ_c draw master curves if plotted against ξ. The master curves depend on c; as c increases, all the mechanical characteristics monotonically increase. If we plot σ_b/υ_{br} and W_b/υ_{br} against G/υ_{br}, the data for various f and φ_c lie on master curves but depending on c. Consequently, the fracture characteristics are not solely described by modulus.

Keywords
Coarse-grained simulations; rubbers; gels; mechanical properties; rupture

Introduction

More needs to be clarified about which structural characteristics dominate the fracture of polymer networks[1]. A few theoretical attempts have been reported focusing on the effect of loops and crack propagation. Barney et al.[2] have extended the real elastic network theory (RENT)[3] to describe the fracture energy. RENT elaborately describes the effect of loops on modulus, considering not only

primary loops (trivial loops) but also higher-order loops; here, a primary loop means a linear chain with the chain ends connected to a single branch point and does not sustain stress. In contrast, secondary and higher-order loops contribute to stress because they are closed structures consisting of some branch points. Combining such a loop-dependent modulus and the Lake-Thomas theory[4], Barney et al. [2] proposed a theoretical expression of the work for crack propagation in tearing tests. They demonstrated that the theoretical prediction is consistent with coarse-grained molecular simulations, in which they varied the conversion ratio and the strand molecular weight. (Here, the conversion ratio means the ratio of reacted chain ends of prepolymers to their total number, including unreacted ones.) Lin and Zhao[5] reported a different theoretical attempt in which they calculated fracture energy considering crack tip propagation. According to this theory, fracture energy increases with secondary loops (cyclic loops) increase, contradicting Barney et al. [2] Wang et al.[6] extended the Lake-Thomas theory according to the work for the opening of a loop at the crack tip considering the roles of unbroken portion[7]. Their fracture energy increases with the number of prepolymers and branch points in the subjected loop.

Several experimental results have been reported that these theories cannot describe. For instance, Akagi et al.[8] observed the fracture of tetra-PEG gels created with various conversion ratios and prepolymer concentrations. Because their networks are made from mixtures of star polymers where each molecule reacts only with the other, primary and higher odd-ordered loops (i.e., circles formed by an odd number of prepolymers) are excluded. Although they observed fracture under uniaxial stretch without an initial notch, the fracture energy and modulus correlate for gels with various conversion ratios, similar to the Lake-Thomas theory. However, the prepolymer concentration dependence is not solely described by modulus. The other example reported by Fujiyabu et al.[9] is that gels made from 3-arm star prepolymers exhibit better fracture properties than those for 4-arm analogs, even if the modulus is the same. They explained this difference by stretch-induced crystallization of the 3-arm case. However, Masubuchi et al.[10] demonstrated that the superiority of 3-arm gels is seen even without crystallization by coarse-grained molecular simulations.

An interesting clue for network fracture is cycle rank. Masubuchi et al.[11] performed coarse-grained simulations for elastic networks prepared from star branch prepolymers to obtain strain and stress at break and work for fracture under uniaxial elongations. They found that for the networks with various branch functionalities (i.e., the number of branching arms for star prepolymers for this specific case) and conversion ratios with monodisperse arm length, some fracture characteristics follow master curves if plotted against cycle rank. Masubuchi[12] also showed that fracture characteristics for networks created from mixtures of star polymers with different functionalities lie on the same master curves as those made from monodisperse sols. In the subsequent work, Masubuchi[13] further examined end-

linking networks composed of linear prepolymers and multi-functional linkers to report that the relationship between fracture characteristics and cycle rank is essentially the same as that for star polymer networks despite including primary and higher-order loops.

This study used phantom chain simulations to explore the relationship between fracture properties and cycle rank for cases with different prepolymer concentrations. Consistent with earlier studies[1,10,14–16], the simulation results showed that modulus and work for fracture increase with increasing prepolymer concentration. The master curves concerning the relation between fracture properties and cycle rank hold for various prepolymer functionalities and conversion ratios. However, they depend on prepolymer concentration in a different manner from that of modulus. Details are shown below.

Model and Simulations

The employed model and simulation scheme are shared with the previous studies[10–13,17] , except for the prepolymer density. Examined networks were created from equilibrated sols of phantom star chains with various concentrations through the Brownian simulations with end-linking reactions. The obtained networks were energy-minimized and stretched until the break. During the elongation, the evolution of stress was recorded as a function of strain, and from the stress-strain relationship thus obtained, the fracture characteristics were extracted. For technical details, see the previous work[10] and its SI.

The prepolymers are represented by bead-spring chains, for which f-arms are connected to the central bead. Since we only deal with end-linking reactions, f corresponds to the functionality of nodes in the resultant networks. The bead number of each arm is N_a. A sufficiently large number of prepolymers M were dispersed with several bead number densities ρ in cubic simulation boxes with periodic boundary conditions and equilibrated via the Brownian dynamics. The equation of motion for the position of each bead $\mathbf{R}_i$ is written as follows.

$$\mathbf{0} = -\zeta\dot{\mathbf{R}}_i + \frac{3k_BT}{a^2}\sum_k f_{ik}\mathbf{b}_{ik} + \mathbf{F}_i \qquad (1)$$

The first term on the right-hand side is the drag force, and ζ is the friction coefficient. The second term is the elastic force generated by springs. Here, a is the average bond length, $\mathbf{b}_{ik}$ is the bond vector defined as $\mathbf{b}_{ik} \equiv \mathbf{R}_i - \mathbf{R}_k$ and f_{ik} is the non-linear spring constant written as $f_{ik} = (1 - \mathbf{b}_{ik}^2/b_{\max}^2)^{-1}$ with the maximum stretch $b_{\max}$. This non-linear spring constant with finite extensibility avoids bond extension due to thermal fluctuations. k_B is the Boltzmann constant, and T is temperature. The third term is Gaussian random force that obeys the fluctuation-dissipation relation with the first term. Since no inter-bead interactions are considered, chain overlapping and crossing are allowed. For the employed model, units of length, energy, and time are defined from this Brownian scheme as a, k_BT,

and $\tau = \zeta a^2/k_BT$. The quantities are normalized according to these units hereafter. Eq 1 was numerically integrated by a second-order scheme[18] with the step size Δt.

After sufficient equilibration, end-linking reactions were turned on[19,20]. Following the experiments for tetra-PEG type gels[1,14], the prepolymers were binary labeled, and the reaction took place only between prepolymers having different labels. Thus, no primary and higher odd-order loops were included in the network, whereas secondary and higher even-order loops were naturally created. The reaction occurs with the reaction rate p when a pair of reactive ends come closer than the critical distance r_c. During the gelation, snapshots of the system with various conversion ratios φ_c were stored. Here, the conversion ratio is defined as $\varphi_c \equiv N_{re}/(Mf)$ with the number of reacted chain ends N_{re}.

The networks thus obtained for various combinations of (ρ,f,φ_c) values were uniaxially stretched under volume conservation. The stretch was performed for energy-minimized networks, as conducted in earlier studies[21–24]. The total energy is written below and is consistent with the non-linear spring employed in the Brownian scheme.

$$U = -\frac{3k_BTb_{\max}^2}{2a^2}\sum_{i,k}\ln\left(1-\frac{\mathbf{b}_{ik}^2}{b_{\max}^2}\right) \qquad (2)$$

This energy was minimized with the Broyden-Fletcher-Goldfarb-Sanno method[25], in which the beads were moved within an infinitesimal distance Δr without Brownian motion according to the potential gradient until the total energy converged to a specific value within a given allowance Δu. In the energy-minimized structure, elongated bonds were removed when the bond length exceeded a certain critical length b_c. The energy-minimization and stretch steps were alternatively repeated until the network percolation was eliminated.

The advantage of the employed energy-minimized scheme is that the results are not affected by the number of parameters, such as the elongation rate and bond-cutting criterion, as discussed previously[10]. The drawback is the lack of thermal motion, and we cannot discuss the energy dissipation according to the structural relaxation[26].

Since the primary purpose of this study is to discuss the effect of prepolymer concentration, the bead number density ρ was varied to 2, 4, and 16, and the results shall be compared with those for the case of $\rho = 8$ examined in the previous study[11]. The number of branching arms, i.e., the node functionality, was varied in a range of $3 \le f \le 8$, and the number of beads on each arm was fixed at $N_a = 5$. For the case of $f = 3$ and $N_a = 5$, the density corresponds to $1 \lesssim c/c^* \lesssim 8$ with respect to the overlapping concentration c^*. Due to the $f-$ dependence of gyration radius, the range is $1.3 \lesssim c/c^* \lesssim 11$ for $f = 8$. The number of prepolymers was fixed at $M = 1600$. The other parameters were the same as in the

previous studies. $\Delta t = 0.01$, $b_{max} = 2$, $b_c = \sqrt{1.5}$, $p = 0.1$, $r_c = 0.5$, $0.6 \leq \varphi_c \leq 0.95$, $\Delta r = 0.01$, and $\Delta u = 10^{-4}$. Eight independent simulation runs were performed for each condition, and the quantities reported below are ensemble averages unless stated.

Results and Discussion

Figure 1 (a) shows snapshots of examined networks before and after energy minimization for $f = 4$ at $\varphi_c = 0.95$ with various ρ values. Since the number of prepolymers M is fixed at 1600, the simulation box size decreases with increasing ρ. Even for the largest ρ with the smallest box case, the box dimension is large enough compared to prepolymers; the box size is ca. 12.8^3 for $f = 4$, whereas the average end-to-end distance is $\sqrt{10}$. Note that M=1600 is sufficient for fracture simulations, as demonstrated previously[10]. Nevertheless, the effect of system size shall be discussed later.

Concerning the network structure, density inhomogeneity due to kinetic arrest is observed when the polymer concentration is low, as experimentally reported earlier[27]. See Fig 1 (b), which shows the radial distribution functions for network nodes $g(r)$. As ρ decreases, $g(r)$ increases, as seen for broken curves showing the data before energy minimization. After energy minimization, the inhomogeneity is enhanced, as indicated by solid curves. Figure 1 (c) exhibits strand length distribution, $P(r)$. Despite spatial inhomogeneity observed for $g(r)$, $P(r)$ before energy minimization shown by broken curves implies the Gaussian distribution of strand length. The energy minimization shrinks such strands, and in the resultant networks, the peak position of $P(r)$ shifts towards smaller r as ρ decreases. Note, however, that $P(r)$ is insensitive to ρ in the long-tail region, implying that the prediction of bond breakage from this distribution is not trivial. The network structures thus obtained are similar to those reported in earlier studies[21–24].

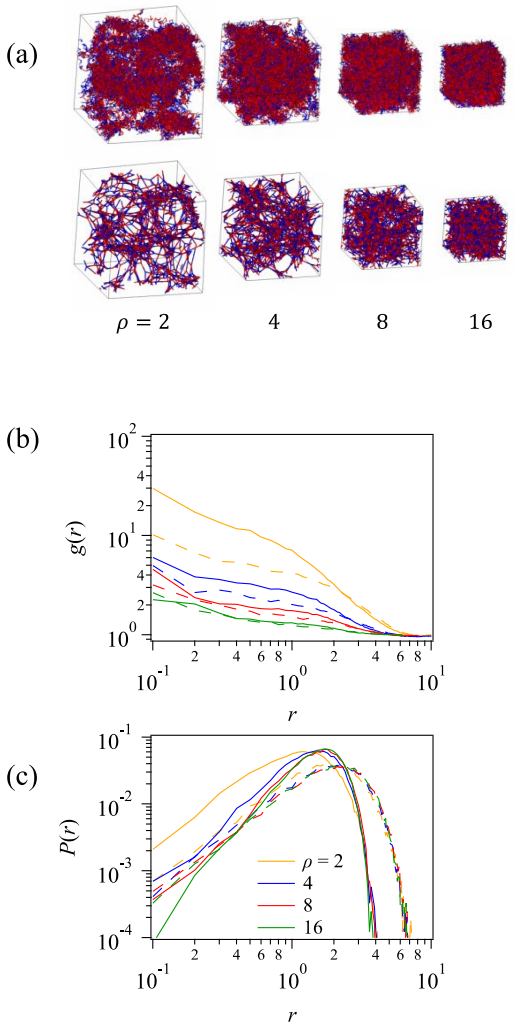

Figure 1 Typical snapshots of examined networks after gelation (top) and after energy minimization (bottom) (a), the radial distribution of network nodes (b), and the strand length distribution (c). $f = 4$, $\varphi_c = 0.95$, and $\rho = 2$, 4, 8, and 16. In panel (a), blue and red indicate different chemistries between which the end-linking reaction occurs. In panels (b) and (c), yellow, blue, red, and green curves exhibit the results for $\rho = 2$, 4, 8, and 16, respectively. Broken and solid curves are the results before and after energy minimization.

Figure 2 shows cycle rank ξ as a function of φ_c. Following the earlier studies[28–30], ξ is defined as the difference between the number of nodes and strands per prepolymer connected to the percolated network, ν and μ. Such values can be directly obtained from simulation snapshots. Meanwhile, in the mean-field theory[28–30], these values are calculated from the probability of finding an arm of prepolymer being excluded from the percolated network p_{out}, which is written as follows.

$$p_{out}(f,\varphi_c) = \varphi_c {p_{out}}^{f-1} + (1-\varphi_c) \qquad (3)$$

The first term on the right-hand side is the probability for the condition in which the subjected arm is reacted, and the other arms of the same polymer are excluded from the percolated network. The second term is the probability of finding the subjected arm unreacted. $p_{out}(f,\varphi_c)$ can be numerically determined for given f and φ_c under the condition $0 \le p_{out} \le 1$. From p_{out}, the probability of finding a prepolymer having h-arms connected to the percolated network, $p_{eff}(f,\varphi_c,h)$, can be calculated as follows.

$$p_{eff}(f,\varphi_c,h) = \binom{f}{h}(1-p_{out})^{h} {p_{out}}^{f-h} \quad (4)$$

Here, $\binom{f}{h}$ is the binomial coefficient. Using p_{eff}, ξ is calculated via ν and μ as follows.

$$\nu(f,\varphi_s) = \sum_{h=3}^{f} h p_{eff}(f,\varphi_c,h) \quad (5)$$

$$\mu(f,\varphi_s) = \sum_{h=3}^{f} p_{eff}(f,\varphi_c,h) \quad (6)$$

$$\xi = \nu - \mu \quad (7)$$

Figure 2 demonstrates that ξ of simulated networks (shown by symbols) does not depend on ρ, and the φ_c-dependence is entirely consistent with the mean-field theory[28–30], as previously reported[11] for the case of $\rho = 8$. This coincidence demonstrates that each reaction occurs independently despite structural inhomogeneity in Fig 1. However, the correspondence of ξ among the networks with different ρ does not mean the maturity of the effective network. Namely, inert fractions like dangling domains are not discriminated in calculating ξ, as discussed later.

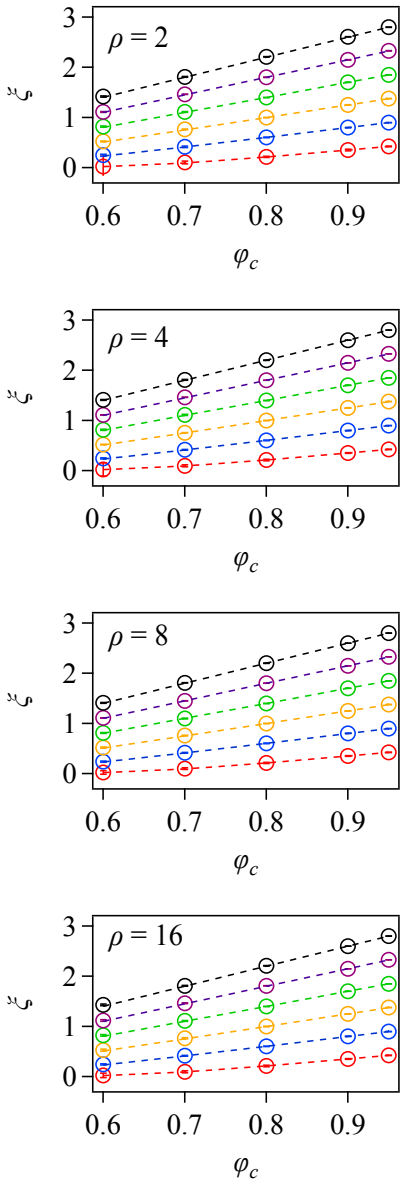

Figure 2 Cycle rank per branch point ξ plotted against φ_c for $\rho = 2$, 4, 8, and 16 from top to bottom with $f = 3$ (red), 4 (blue), 5 (orange), 6 (green), 7 (violet), and 8 (black). Dotted curves indicate the mean-field calculation. Error bars (within symbols) show the standard deviation of 8 different simulation runs. Note that the results for $\rho = 8$ were reported previously.

Figure 3 shows examples of the development of true stress σ during elongation against true strain ε. For this specific case, $f = 4$, $\varphi_c = 0.95$, and $\rho = 2$, 4, 8, and 16. The modulus G increases with increasing ρ since the density of effective strands increases. During elongation, stress fluctuates, reflecting the breakage of some strands. Owing to the energy-minimization scheme, stress immediately goes down to zero when network percolation is eliminated. Conversely, energy dissipation due to network relaxation[26] is not considered. Nevertheless, in addition to modulus (G),

strain and stress at break (ε_b and σ_b) and work for fracture (W_b) were obtained from each stress-strain curve. (Note that W_b here is energy per unit volume, and is different from the fracture energy in tearing experiments defined as energy per unit area.) These values were averaged among 8 independent simulations for various ρ, f, and φ_c, and the data are shown below.

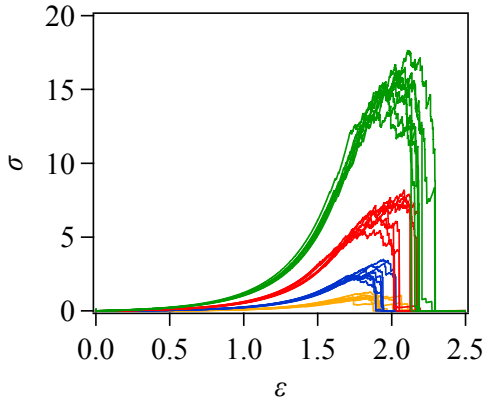

Figure 3 True stress versus true strain during elongation for $f = 4$ and $\varphi_c = 0.95$. The results for $\rho = 2$, 4, 8, and 16 are shown by orange, blue, red, and green curves, respectively. Each curve corresponds to a single simulation run.

Figure 4 shows the modulus G plotted against ρ for $\varphi_c = 0.6$ (top) and 0.95 (bottom) with various f. The modulus was obtained as the value of $\sigma/(\lambda^2 - \lambda^{-1})$ with the stretch λ at $\lambda^{-1} = 0.75$, as in the previous study[11]. As mentioned in Fig 3, G increases with increasing ρ. However, G is not proportional to ρ for low ρ. See the deviation from the dotted lines that indicate the slope of unity. This non-linearity of G against ρ reflects that some fractions of network nodes do not effectively sustain stress.

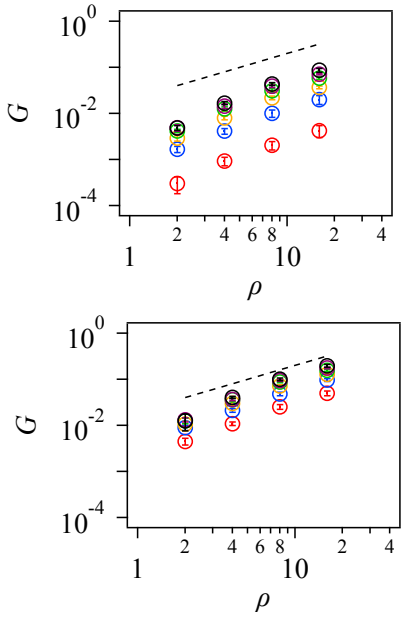

Figure 4 Modulus G plotted against ρ for $f = 3$ (red), 4 (blue), 5 (orange), 6 (green), 7 (violet), and 8

(black) at $\varphi_c = 0.6$ (top) and 0.95 (bottom). Broken lines indicate the slope of unity. Error bars correspond to the standard deviations for 8 different simulation runs.

Figure 5 (a) shows G normalized by the number density of branch points υ_{br} plotted against cycle rank ξ for various ρ. υ_{br} is defined as $\upsilon_{br} \equiv M/V = \rho/(fN_a + 1)$ with the volume V, and unreacted prepolymers and dangling ones are not excluded. The data obtained for various f and φ_c lie on a master curve depending on ρ, and G/υ_{br} decreases with decreasing ρ. G/υ_{br} is not proportional to ξ, but it indicates weak non-linearity for small ξ. These discrepancies from the phantom network theory[31] are due to the network maturity; some strands in the percolated network do not contribute to stress. Indeed, Figure 5 (b) shows consistency with the phantom network theory [31]; all the G/υ_{br} data from different f, φ_c, and ρ values converge to a single line within the error if they are plotted against the effective cycle rank ξ_{eff}, which is obtained from the numbers of nodes and strands actually sustaining stress. As seen in Figure 5 (c), ξ_{eff} increases with increasing ρ, implying that the network maturity depends on ρ, and the modulus reflects it.

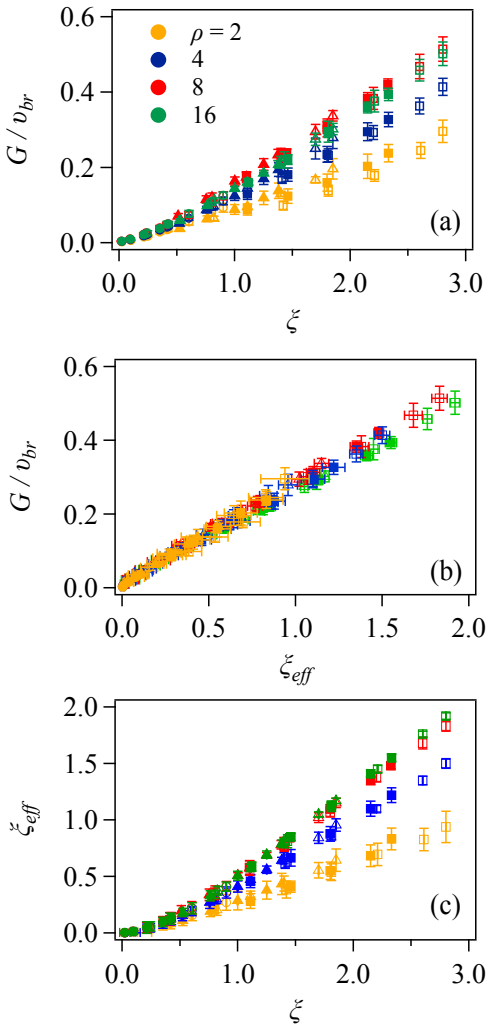

Figure 5 Modulus G normalized by the number density of branch points υ_{br} as a function of cycle rank ξ (a), G/υ_{br} plotted against effective cycle rank ξ_{eff} (b) and ξ_{eff} versus ξ (c). Yellow, blue, red, and green symbols indicate the results for the bead density ρ at 2, 4, 8, and 16, respectively. Symbols indicate $f = 3$ (filled circle), 4 (unfilled circle), 5 (filled triangle), 6 (unfilled triangle), 7 (filled square), and 8 (unfilled square), respectively. Error bars indicate the standard deviations for 8 different simulation runs.

Figure 6 shows the fracture characteristics plotted against ρ for $\varphi_c = 0.6$ (left column) and 0.95 (right column). Concerning ε_b, stretch at break $\lambda_b (= \exp(\varepsilon_b))$ is shown in panels (a1) and (a2). Akagi et al.[8] reported for tetra-PEG gels ($f = 4$) with φ_c~0.9 that λ_b exhibits a power-law dependence on the prepolymer concentration φ with the power-law exponent of 1/3 ($\lambda_b \sim \varphi^{1/3}$). Assuming that φ is proportional to ρ, we add broken lines with a slope of 1/3 in panels (a1) and (a2). The simulation results indicated by symbols are inconsistent with this relation. For the case of $\varphi_c = 0.6$ (panel a1), λ_b is almost constant within the examined range of ρ for $f > 3$. For $f = 3$ (red symbol), λ_b significantly

decreases with increasing ρ. This behavior is probably due to the difference in φ_c; any experimental reports for networks with such a low conversion ratio cannot be found. However, the discrepancy is also seen for $\varphi_c = 0.95$ (see panel (a2)). A possible reason is explained as follows. In the experiment, polymers are dispersed in a good solvent, and gel networks swell due to osmotic pressure. Such a swelling attains the development of a mechanically effective network with relatively homogeneous structures, even under low polymer concentrations. In contrast, our simulations are for phantom chains, and the effect of osmotic force is neglected. Thus, when the prepolymer concentration is low, structural inhomogeneity is enhanced as the reaction proceeds, as seen in Fig 1. The mechanical behaviors reflect this structural difference, at least partly. Note that even for tetra-PEG gels, structural inhomogeneity is observed when prepolymer concentration is extremely low[27].

Figure 6 panels b and c exhibit σ_b and W_b plotted against ρ for various f, demonstrating that these fracture characteristics increase with increasing ρ. Even though the simulation setting is different from tearing tests, if we assume the Lake-Thomas theory and regard W_b as a quantity comparable to the fracture energy, W_b is expected to be proportional to ρ. Broken lines in panels (c1) and (c2) show this behavior, and the simulation results shown by the symbols are qualitatively consistent. However, some discrepancies are also observed. For instance, the ρ-dependence of W_b is somewhat more intense than the broken line when ρ is low and f is large. W_b for the case with $f = 3$ and $\varphi_c = 0.6$ (red circle in panel c1) saturates in high ρ regime. Note, however, that the fracture energy in tearing tests is defined as energy per unit area, whereas W_b here is energy per unit volume; thus, straightforward comparison is difficult.

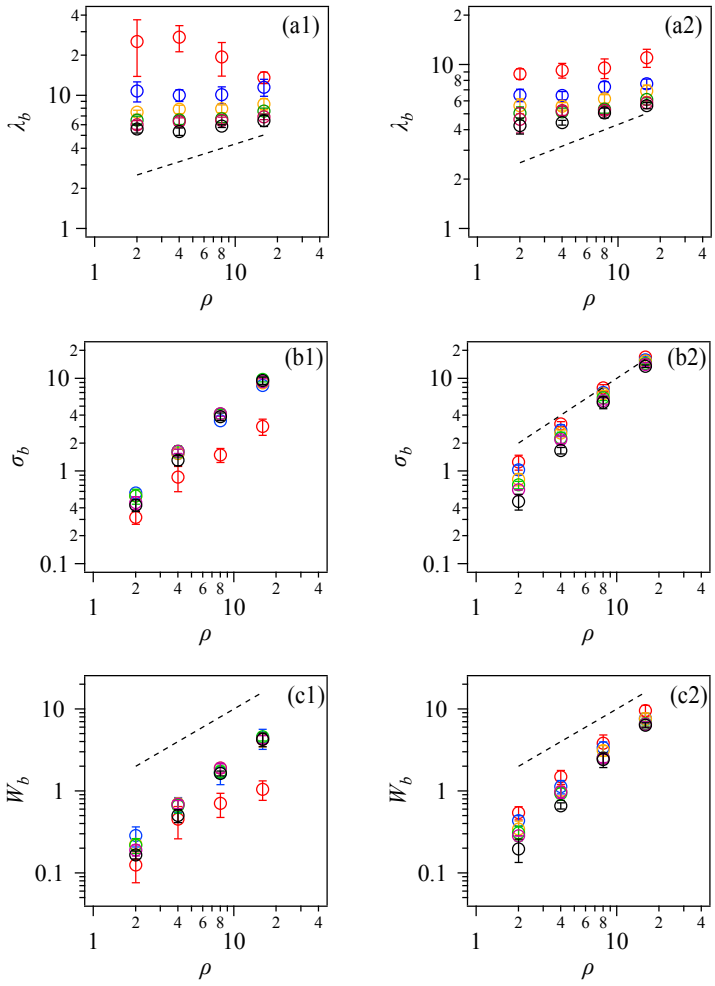

Figure 6 Stretch at break $\lambda_b \equiv \exp(\varepsilon_b)$(panels a), stress at break σ_b (panels b), and work for fracture W_b (panels c) plotted against the bead number density ρ at $\varphi_c = 0.6$ (left column) and 0.95 (right column) for $f = 3$ (red), 4 (blue), 5 (orange), 6 (green), 7 (violet), and 8 (black). Error bars correspond to the standard deviations for 8 different simulation runs. Broken curves in panels a and c indicate slopes of 1/3 and unity.

One might argue that the results depicted in Fig. 6 reflect not just the effect of density but also of system size, given that the simulation box dimensions varied, as shown in Fig. 1. For this matter, we present results with a fixed box dimension, filled with varying numbers of molecules. Figure 7 illustrates ε_b, σ_b, and W_b for $f = 4$ at $\varphi_c = 0.6$ and 0.95, across various ρ, with a constant box volume. The results align with those in Fig. 6, where the number of molecules was fixed, thereby indicating that the effect of system size is insignificant.

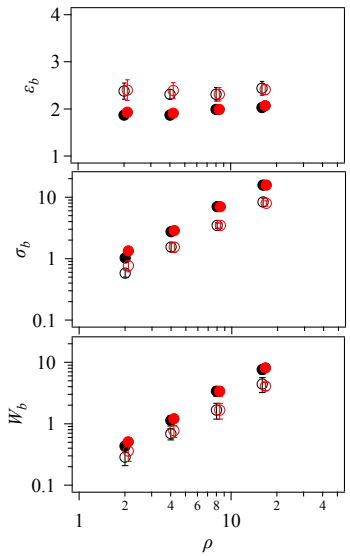

Figure 7 Strain at break ε_b, stress at break σ_b, and work for fracture W_b from top to bottom plotted against the bead number density ρ for $f = 4$ at $\varphi_c = 0.6$ (unfilled circle) and 0.95 (filled circle) for the simulation with a constant volume (red) and with a constant prepolymer number (black). For the constant volume simulation, the volume V was fixed at 4200, and the number of prepolymers M was varied as 400, 800, 1600, and 3200. For the simulation with the constant prepolymer number, $M = 1600$ and $V =$ 16800, 8400, 4200, and 2100. Error bars correspond to the standard deviations for 8 different simulation runs and are sometimes smaller than the symbols. To avoid overlaps, red and black symbols are shown with horizontal offsets.

Figure 8 exhibits all the obtained fracture characteristic values for various sets of ρ, f, and φ_c plotted against ξ. For each ρ, ε_b data in panel (a) are located on a master curve described as a power-law decay function of ξ; $\varepsilon_b = A_\varepsilon \xi^{-\alpha_\varepsilon}$. The power-law dependence can be confirmed in the double logarithmic plot exhibited in the right panel. As ρ increases, ε_b slightly increases systematically. As reported previously[11–13], σ_b and W_b for various f and φ_c also lie on master curves if these values divided by υ_{br} are plotted against ξ. In a similar manner with ε_b, these behaviors are described by power-law functions of ξ; $\sigma_b/\upsilon_{br} = A_\sigma \xi^{\alpha_\sigma}$ and $W_b/\upsilon_{br} = A_W \xi^{\alpha_W}$. As ρ increases, both σ_b/υ_{br} and W_b/υ_{br} increase. The master curves have been previously reported for $\rho = 8$, but they are found for the first time for the other ρ values. Note that in the previous study[11], σ_b and W_b were normalized by the broken strand fraction φ_{bb}. However, the value of φ_{bb} is hardly experimentally accessible, and υ_{br} was found to achieve the master curves instead of φ_{bb} in the other previous study[13].

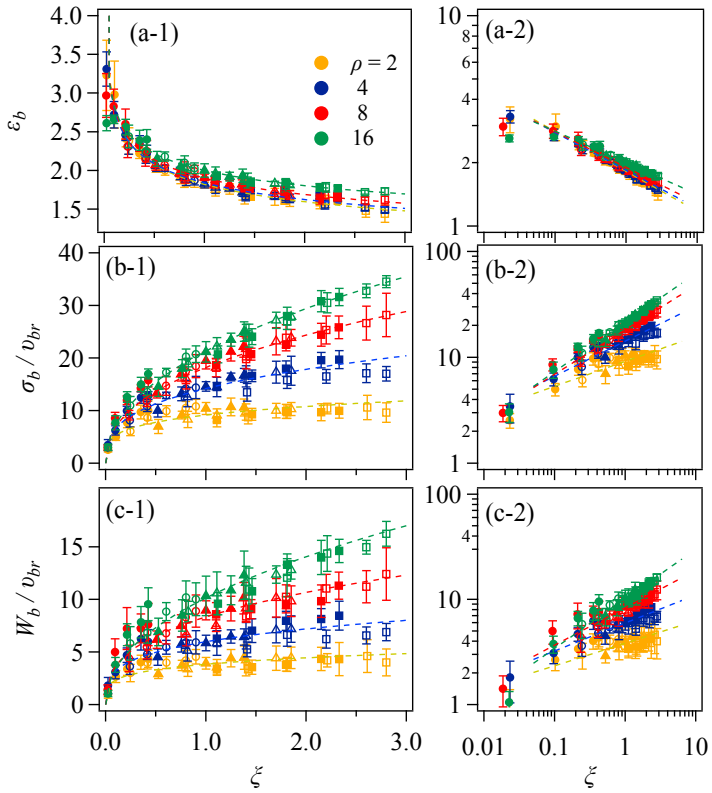

Figure 8 Fracture characteristics ε_b, σ_b, and W_b obtained for various ρ, f, and φ_c values as functions of ξ. σ_b and W_b are normalized by the branch point density υ_{br}. The right panels show logarithmic plots. The f values are 3 (filled circle), 4 (unfilled circle), 5 (filled triangle), 6 (unfilled triangle), 7(filled square), and 8 (unfilled square), respectively. Error bars are standard deviations among eight different simulation runs. Broken curves show power-law functions; $\varepsilon_b = A_\varepsilon \xi^{-\alpha_\varepsilon}$, $\sigma_b/\upsilon_{br} = A_\sigma \xi^{\alpha_\sigma}$ and $W_b/\upsilon_{br} = A_W \xi^{\alpha_W}$.

Figure 9 exhibits the parameters for the power-law functions plotted against ρ. Reflecting the weak $\rho-$dependence of ε_b in Fig 8, the power-law exponent α_ε and the factor A_ε vary against ρ only slightly. The exponents for σ_b/υ_{br} and W_b/υ_{br} are similar and increase with increasing ρ, as seen in Fig 8. The change against ρ is similar also for the factors.

We emphasize that the power-law fittings in Fig 8 are just for eye guidance. Since no theoretical explanation has been found at present, better functional forms may exist to fit the data. Specifically, the fracture characteristics must be lower-limited due to a minimum stretch below which fracture does not occur. The power-law expressions are not compatible with such an intuition.

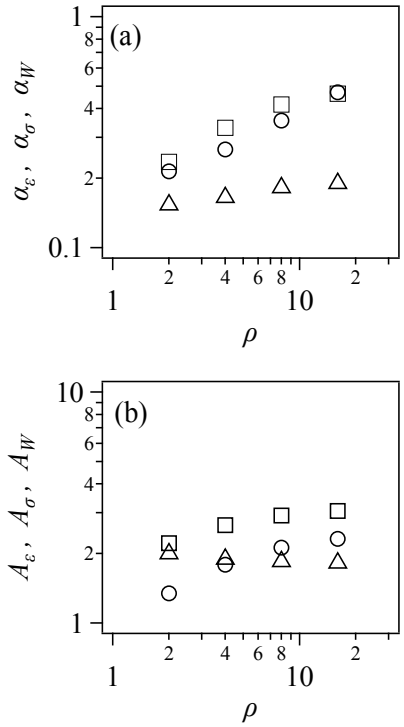

Figure 9 Parameters employed for the power-law fittings in Fig 8; the power-law exponents (a) and the factors (b) plotted against ρ. Triangle, square, and circle show the parameters for ε_b, σ_b, and W_b, respectively.

One may argue that Figures 5 and 8 suggest a correlation between the modulus and the fracture characteristics. Figure 10 examines such an argument. For each ρ case, σ_b/υ_{br} and W_b/υ_{br} are single-valued functions of G/υ_{br}. Namely, the fracture behavior for the networks with various f and φ_c is dominated by the modulus, given that ρ is common. However, when ρ differs, networks sharing the same G/υ_{br} value exhibit different σ_b/υ_{br} and W_b/υ_{br} values; these values increase with increasing ρ. Consequently, the fracture characteristics are not solely described by modulus. These results are consistent with the experiment by Fujiyabu et al. [9], who demonstrated that tetra-PEG and tri-PEG gels exhibit different fracture characteristics even if the modulus is tuned to be common. Note that the results in Figs 5 and 10 also imply that the curves in Fig 8 do not converge to a single curve even if the values are plotted against ξ_{eff}; according to Fig 5 (b), a plot against G/υ_{br} is essentially the same as that against ξ_{eff}.

The results shown in Fig 10 imply that network maturity evaluated by modulus differs from that affects fracture properties. Modulus is used to quantify the density of effective strands and nodes, and their mechanical contributions appear as an averaged value. In contrast, the fracture is initiated by the scission of the most elongated strand and propagates to the next ones in a cascade manner. Since we

conducted simulations with step-by-step energy minimization, this propagation occurs within the elongated tail of the strand length distribution. Therefore, modulus and fracture reflect different characteristics of the strand length statistics that are unnecessarily correlated.

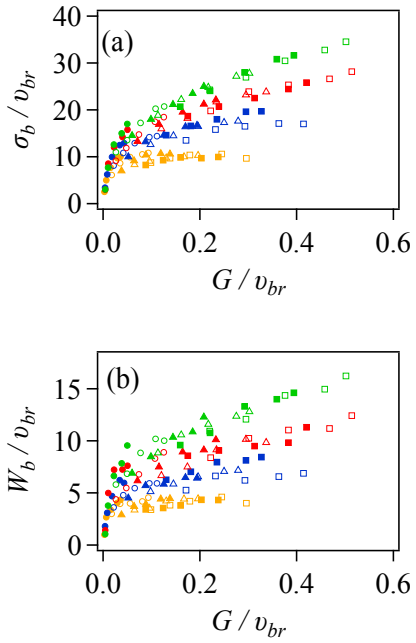

Figure 10 Fracture characteristics σ_b/υ_{br} (a) and W_b/υ_{br} (b) obtained for various ρ, f, and φ_c values plotted against G/υ_{br}. The f values are 3 (filled circle), 4 (unfilled circle), 5 (filled triangle), 6 (unfilled triangle), 7(filled square), and 8 (unfilled square), respectively. The ρ values are 2 (yellow), 4 (blue), 8 (red), and 16 (green), respectively.

Conclusions

We conducted phantom chain simulations to investigate the effect of prepolymer concentration on the fracture behavior of star polymer networks. We varied the star polymer functionality f from 3 to 8, the conversion ratio φ_c from 0.6 to 0.95, and the segment number density ρ from 2 to 16. The resultant networks were statistically evaluated regarding the cycle rank ξ, which was consistent with the mean-field theory, demonstrating that the end-linking reactions occurred independently. We uniaxially stretched the networks and obtained modulus G and fracture characteristics, including strain at break ε_b, stress at break σ_b, and work for fracture W_b from the stress-strain relation until the break. Consistent with experiments, these mechanical characteristics increase with increasing ρ. With the branch point density υ_{br}, if we plot G/υ_{br}, ε_b, σ_b/υ_{br}, and W_b/υ_{br} against ξ, the data for various f and φ_c are located on master curves, as reported previously. However, different curves are realized for different ρ values. We also found that if we plot σ_b/υ_{br} and W_b/υ_{br} against G/υ_{br}, master curves are seen for various f and φ_c, but they depend on ρ. This result demonstrates that fracture is not solely

dominated by modulus but depends on prepolymer density.

Although the presented study gives fundamental information about network fracture, it is fair to note that the reported ξ-dependence of fracture characteristics has not been experimentally confirmed. The reason is that few datasets report fractures of networks with a sufficient range of f and φ_c. In particular, φ_c needs to be clarified in most literature. We should also note that the results may change if we consider osmotic force, excluded volume interactions, and thermal fluctuations. Besides, we have not found any interpretation of the significance of cycle rank, which may be better converted to other structural parameters that include the opening loop length[6] and the minimum path length[32]. Subsequent works toward such directions are ongoing, and the results will be reported elsewhere.

Acknowledgments

This study is partly supported by JST-CREST (JPMJCR1992) and JSPS KAKENHI (22H01189).

References

1 Takamasa. Sakai, *Physics of Polymer Gels*, Wiley, 2020.

2 C. W. Barney, Z. Ye, I. Sacligil, K. R. McLeod, H. Zhang, G. N. Tew, R. A. Riggleman and A. J. Crosby, *Proceedings of the National Academy of Sciences*, 2022, **119**, 2–7.

3 M. Zhong, R. Wang, K. Kawamoto, B. D. Olsen and J. A. Johnson, *Science (1979)*, 2016, **353**, 1264–1268.

4 J. Lake and A. G. Thomas, *Proc R Soc Lond A Math Phys Sci*, 1967, **300**, 108–119.

5 S. Lin and X. Zhao, *Phys Rev E*, 2020, **102**, 52503.

6 S. Wang, C. M. Hartquist, B. Deng and X. Zhao, *Macromolecules*, 2024, **57**, 6069–6075.

7 S. Wang, S. Panyukov, S. L. Craig and M. Rubinstein, *Macromolecules*, 2023, **56**, 2309–2318.

8 Y. Akagi, T. Katashima, H. Sakurai, U. Il Chung and T. Sakai, *RSC Adv*, 2013, **3**, 13251–13258.

9 T. Fujiyabu, N. Sakumichi, T. Katashima, C. Liu, K. Mayumi, U. Chung and T. Sakai, *Sci Adv*, 2022, **8**, abk0010_1-abk0010_10.

10 Y. Masubuchi, Y. Doi, T. Ishida, N. Sakumichi, T. Sakai, K. Mayumi and T. Uneyama, *Macromolecules*, 2023, **56**, 2217–2223.

11 Y. Masubuchi, Y. Doi, T. Ishida, N. Sakumichi, T. Sakai, K. Mayumi, K. Satoh and T. Uneyama, *Macromolecules*, 2023, **56**, 9359–9367.

12 Y. Masubuchi, *Polym J*, 2024, **56**, 163–171.

13 Y. Masubuchi, *Polymer (Guildf)*, 2024, **297**, 126880.

14 T. Sakai, *Nihon Reoroji Gakkaishi*, 2019, **47**, 183–195.

15 M. Shibayama, X. Li and T. Sakai, *Colloid Polym Sci*, 2019, **297**, 1–12.

16 T. Sakai, Y. Akagi, S. Kondo and U. Chung, *Soft Matter*, 2014, **10**, 6658–6665.

17 Y. Masubuchi, *Nihon Reoroji Gakkaishi*, 2024, **52**, 21–26.

18 R. L. Honeycutt, *Phys Rev A (Coll Park)*, 1992, **45**, 600–603.

19 Y. Masubuchi, R. Yamazaki, Y. Doi, T. Uneyama, N. Sakumichi and T. Sakai, *Soft Matter*, 2022, **18**, 4715–4724.

20 Y. Masubuchi and T. Uneyama, *Soft Matter*, 2019, **15**, 5109–5115.

21 M. Lang, *Macromolecules*, 2019, **52**, 6266–6273.

22 K. Nishi, H. Noguchi, T. Sakai and M. Shibayama, *J Chem Phys*, 2015, **143**, 184905.

23 K. Nishi, M. Chijiishi, Y. Katsumoto, T. Nakao, K. Fujii, U. Chung, H. Noguchi, T. Sakai and M. Shibayama, *J Chem Phys*, 2012, **137**, 224903.

24 J. Lei, Z. Li, S. Xu and Z. Liu, *J Mech Phys Solids*, 2021, **156**, 104599.

25 J. Nocedal, *Math Comput*, 1980, **35**, 773.

26 A. Arora, T. S. Lin and B. D. Olsen, *Macromolecules*, 2022, **55**, 4–14.

27 S. Ishikawa, Y. Iwanaga, T. Uneyama, X. Li, H. Hojo, I. Fujinaga, T. Katashima, T. Saito, Y. Okada, U. Chung, N. Sakumichi and T. Sakai, *Nat Mater*, 2023, **22**, 1564–1570.

28 C. W. Macosko and D. R. Miller, *Macromolecules*, 1976, **9**, 199–206.

29 C. W. Macosko and D. R. Miller, *Makromol. Chem.*, 1991, **192**, 377–404.

30 Y. Yoshikawa, N. Sakumichi, U. Chung and T. Sakai, *Soft Matter*, 2019, **15**, 5017–5025.

31 H. M. James and E. Guth, *J Chem Phys*, 1943, **11**, 455–481.

32 Z. Yu and N. E. Jackson, , DOI:10.48550/arXiv.2405.03551.